FAST Reveals New Evidence for M94 as a Merger

Ruilei Zhou, Ming Zhu, Yanbin Yang, Haiyang Yu, Lixia Yuan, Peng Jiang, Wenzhe Xi

The Astrophysical Journal, 952:130 (11pp), 2023 August 1 https://doi.org/10.3847/1538-4357/acdcf5

FAST Reveals New Evidence for M94 as a Merger

Ruilei Zhou[1,2,3], Ming Zhu[1,2,3,4], Yanbin Yang[5], Haiyang Yu[1,2,3], Lixia Yuan[6], Peng Jiang[1,3,4], and Wenzhe Xi[2,7]
[1] National Astronomical Observatories, Chinese Academy of Sciences, A20 Datun Road, Beijing 100101, People's Republic of China; mz@nao.cas.cn
[2] University of Chinese Academy of Sciences, Beijing 100049, People's Republic of China
[3] CAS Key Laboratory of FAST, National FAST, National Astronomical Observatories, Chinese Academy of Sciences, Beijing 100101, People's Republic of China
[4] Guizhou Radio Astronomical Observatory, Guizhou University, Guiyang 550000, People's Republic of China
[5] GEPI, Observatoire de Paris, CNRS, Place Jules Janssen F-92195, Meudon, France
[6] Purple Mountain Observatory and Key Laboratory of Radio Astronomy, Chinese Academy of Sciences, 10 Yuanhua Road, Qixia District, Nanjing 210033, People's Republic of China
[7] Yunnan Observatories, Chinese Academy of Sciences, Kunming 650011, People's Republic of China
Received 2023 April 25; revised 2023 June 1; accepted 2023 June 7; published 2023 July 24

Abstract

We report the first high-sensitivity H I observation toward the spiral galaxy M94 with the Five-hundred-meter Aperture Spherical radio Telescope. From these observations, we discovered that M94 has a very extended H I disk, twice larger than that observed by THINGS, which is accompanied by a H I filament and seven high velocity clouds (HVCs) at different distances. The projected distances of these clouds and filaments are less than 50 kpc from the galactic center. We measured a total integrated flux (including all clouds/filament) of 127.3 (± 1) Jy km s^{-1}, corresponding to a H I mass of $(6.51 \pm 0.06) \times 10^8 M_{\odot}$, which is 63.0% more than that observed by THINGS. By comparing numerical simulations with the H I maps and the optical morphology of M94, we suggest that M94 is likely a remnant of a major merger of two galaxies, and the HVCs and H I filament could be the tidal features that originated from the first collision of the merger, which happened about 5 Gyr ago. Furthermore, we found a seemingly isolated H I cloud at a projection distance of 109 kpc without any optical counterpart detected. We discuss the possibilities of the origin of this cloud, such as dark dwarf galaxy and RELHIC (REionization-Limited H I Cloud). Our results demonstrate that high-sensitivity and wide-field H I imaging is important in revealing diffuse cold gas structures and tidal debris, which is crucial to understand the dynamical evolution of galaxies.

Unified Astronomy Thesaurus concepts: Galaxy evolution (594); Galaxy interactions (600); Galaxy kinematics (602); Galaxy dynamics (591); H I regions (693)

1. Introduction

NGC 4736 (=M94) is a nearby bright galaxy at a distance of 4.66 Mpc (Karachentsev 2005), which was classified as a (R) SA(r)ab-type galaxy (de Vaucouleurs et al. 1991) and reclassified as (R)SAB(rs)ab-type by Buta et al. (2007). It is the brightest galaxy of the Canes Venatici I cloud (CVnI) near the center of the CVnI cloud and it is the main disturber relative only to 10 neighboring galaxies (Karachentsev 2005). M94 is the closest example of a LINER 2 nucleus, although whether the LINER 2 is powered by a low-luminosity active galactic nucleus (LLAGN) is uncertain (Roberts et al. 2001).

Multi-wavelength images of M94 have been observed to study its morphology, such as optical (SDSS), UV (Maoz et al. 1995), far-infrared (Smith et al. 1991), near-infrared (2MASS, Jarrett et al. 2003), and 21 cm H I line (THINGS, de Blok et al. 2008). According to Trujillo et al. (2009), NGC 4736 can be divided into five main regions: (a) a bulge ($R < 15''$), (b) an inner ring ($R \approx 45''$), (c) an outer spiral structure with oval stellar distribution ($R \approx 220''$), (d) a zone of low surface brightness, and (e) a faint outer ring ($R \approx 350''$). However, non-optical data suggest that there is a disk with a spiral arm structure rather than a stellar ring in the outer region of NGC 4736, such as H I (Walter et al. 2008, their Figure 51; de Blok et al. 2008, their Figure 80; Braun 1995, his Figure 8), UV (Trujillo et al. 2009, their Figure 2), and infrared (Trujillo et al. 2009, their Figure 2). M94 is a post-starburst galaxy. In FUV, Kinney et al. (1993) found that the off-nuclear continuum is flat with little trace of the emission-like features around 1900 Å seen in the nuclear spectrum, and Waller et al. (2001) thought that this is consistent with an aging burst that is spatially more extended than the centrally concentrated stars of the older disk and bulge. Muñoz-Tuñón et al. (2004) found evidence for a fossil starburst nucleus, which is a kinematically detached innermost area defined by a clear dip in the stellar velocity dispersion with a size about 150 pc. Shioya et al. (1998) observed the post-starburst nucleus of M94 in ^{12}CO ($J = 1 - 0$), and they thought that bar-driven instability fueling or minor-merger driven fueling (or triggering) may be possible scenarios for the nuclear starburst.

Although many studies show that M94 is a rather isolated galaxy (Watkins et al. 2016), there is much evidence that M94 is related to interaction or merger. As a post-starburst galaxy, Maoz et al. (2005) noted a second UV source that is offset from the galaxy nucleus by 2.″5 (~60 pc in projection), and they thought that the off-nuclear could be the active nucleus of a galaxy that had merged with M94. They also suggested that this merger may trigger the past starburst and the peculiar morphological and kinematic features observed in M94. Constantin & Seth (2012) drew a conclusion that M94 may be in the final stage of a merger by comparing the intricate structure of off-nuclear compact source detections in X-ray, radio, and UV. Körding et al. (2005) reported another possibility for the off-nuclear source that could be the result of jet activities in the nucleus. The kinematics of planetary nebulae (PNe) also show evidence of flaring in the old stellar

population (Herrmann & Ciardullo 2009; Herrmann et al. 2009), which may indicate some past perturbation. M94 has a bright anti-truncated outer disk (Trujillo et al. 2009) and its rotation curves decline by ∼30% from the inner region (∼3 kpc) to the outer region (∼9 kpc) (Mulder 1995; de Blok et al. 2008). In the simulations of Peñarrubia et al. (2006), extended disks may be the result of a tidal disrupted dwarf galaxy coplanar with the disk of the host galaxy in prograde orbit, and the kinematic average rotational motion of the stars forming the extended disk is more than 30–50 km s^{-1} lower than the host's circular velocity. Thus, the much declining rotation curve could favor a merger origin for the outer disk of M94. However, if all of the outer disk were entirely the result of a disrupted dwarf, then M94 would have a high merger ratio 1:4 (Trujillo et al. 2009), so we could not ignore the possibility that the accretion destroyed the inner disk (Hopkins et al. 2009). In the merging simulations of massive satellites with disk galaxies (Velazquez & White 1999), the tilt for the outer regions is much smaller than that observed by Trujillo et al. (2009). Trujillo et al. (2009) also found that the specific star formation rate of the outer disk is twice that of the inner disk, and they listed two origins: a merger or an oval distortion in the inner disk. Using numerical simulations, they found that the latter origin provided a good match to the observed structure of M94. Thus ,the existing observational evidence is not enough to prove that M94 has undergone a merger event. To further investigate the evolution history of M94, more high-sensitivity observations are needed.

In this paper, we present a wide-field H I imaging study of M94 with the Five-hundred-meter Aperture Spherical radio Telescope (FAST). Our newly discovered morphological and kinematic features could be used to constrain models for galaxy interactions and evolution. In Section 2, we describe the details of the observations and data reduction. In Section 3, we describe the properties of these H I features in detail and discuss the possible origins of the discoveries in Section 4. Finally, we summarize our results in Section 5. All of the velocities quoted in the paper are heliocentric, unless otherwise specified.

2. Observation and data reduction

Using the FAST (Nan et al. 2011; Jiang et al. 2019; Jiang et al. 2020), we mapped a sky region of R.A. of $191\overset{\circ}{.}57 < \alpha < 193\overset{\circ}{.}84$, decl. of $40\overset{\circ}{.}03 < \delta < 41\overset{\circ}{.}82$ and velocity range of 114.2–504.2 km s^{-1}. FAST is located in Guizhou, China, with 500 m aperture and 300 m illuminated aperture. The observation was carried out with the 19 beam receiver, which has a frequency range from 1050 to 1450 MHz. We selected the Spec(W) spectrometer, which has a bandwidth of 500 MHz and 655,536 channels, corresponding to a spectral resolution of 1.67 km s^{-1}. With a $23\overset{\circ}{.}4$ rotation of the 19 beam receiver platform, the beam tracks are equally spaced in decl. with $1\overset{\prime}{.}14$ spacing. The half-power beamwidth (HPBW) was about $2\overset{\prime}{.}9$ at 1.4 GHz for each beam and the pointing accuracy of FAST was about $12''$.

The data is composed of two parts. Part I was observed on 2021 December 13, 15, 16, 23, 25, and 26, carried out with the drift scan mode. Part II was observed on 2021 May 1, and carried out with the Multibeam on-the-fly (OTF) mode, which focused on the region around M94 to improve the sensitivity to detect weak features outside the M94 disk. We performed flux calibration by injecting a 10 K calibration signal (CAL) every 32 s for a duration of 1 s to calibrate the antenna temperature. The data were reduced using HIFAST (Y. Jing et al. 2023, in preparation) data reduction pipeline. We made baseline correction with the asymmetrically reweighted penalized least-squares algorithm (arsPLs, Baek et al. 2015). After the spectra were fully calibrated, we gridded them into an image with $1'$ spacing, and created the data cube in the standard FITS format. More detailed procedures are described in Xu et al. (2021). The data were then smoothed from 1.67 km s^{-1} velocity resolution to 4.88 km s^{-1}. Since we used the same techniques as HIPASS to calibrate and grid the data, we made flux corrections according to Barnes et al. (2001). The rms brightness temperature sensitivity of Part I is approximately 9.3 mK or 0.6 mJy beam^{-1} per channel, while that of the region with both Part I and II data combined is 6.2 mK or 0.4 mJy beam^{-1} per channel. In the following study, σ refers specifically to the σ of Part II because most features were studied through Part II.

3. Results

3.1. Extended H I Map

The top panel of Figure 1 shows the H I column density distribution of M94 integrated over 114–504 km s^{-1} overlaid with the H I integrated flux density contours detected by the VLA (green) from THINGS (de Blok et al. 2008; Walter et al. 2008). In this figure, the lower right-hand subpanel is integrated over 290–319 km s^{-1} to show a weak H I cloud far away from the central region. The bottom panel shows the same FAST detected contours superimposed on the optical image of M94 from the DESI Legacy Imaging Surveys (DESI-LS; Dey et al. 2019). The THINGS survey has a high spatial resolution (∼6″), which can reveal the detail H I distribution of the galaxy disk, while the FAST data can better show the diffuse H I gas outside the disk. The FAST contour levels starting at 3σ (2.5×10^{18} cm^{-2} for M94 region, and 6.7×10^{17} cm^{-2} for the lower right-hand subpanel) is much lower than that of THINGS map, which is 1.3×10^{20} cm^{-2}. The moment-0 map was made using the spectral-cube algorithm[8] and smoothed by a Gaussian filter (kernel = 3×3). A few obvious bad pixels were masked manually. From Figure 1, we can see that the FAST map reveals a large amount of diffuse H I gas outside the H I disk covered in the THINGS map. The THINGS map covers the central ∼140 arcmin^2 area, while FAST's map covers three times more extended area than that of THINGS, and allows us to detect huge amount of low column density H I gas.

3.2. Total H I Flux

By integrating all the H I flux in Figure 1, including the H I structures discussed in the next section, we measured a total integrated flux of 127.3(±1)Jy km s^{-1}, or H I mass of $(6.51 \pm 0.06) \times 10^8 M_\odot$ for M94. Within the region covered by THINGS, the integrated flux observed by FAST is 97.0 Jy km s^{-1}, while that from THINGS measurement (Walter et al. 2008) is 78.1 Jy km s^{-1} (after correcting for primary beam attenuation). Thus, the total integrated flux observed by FAST is 63.0% larger than that of observed by THINGS. In the area overlapping with THINGS observation, 24.2% of the fluxes

[8] https://spectral-cube.readthedocs.io/en/latest/moments.html#moment-maps

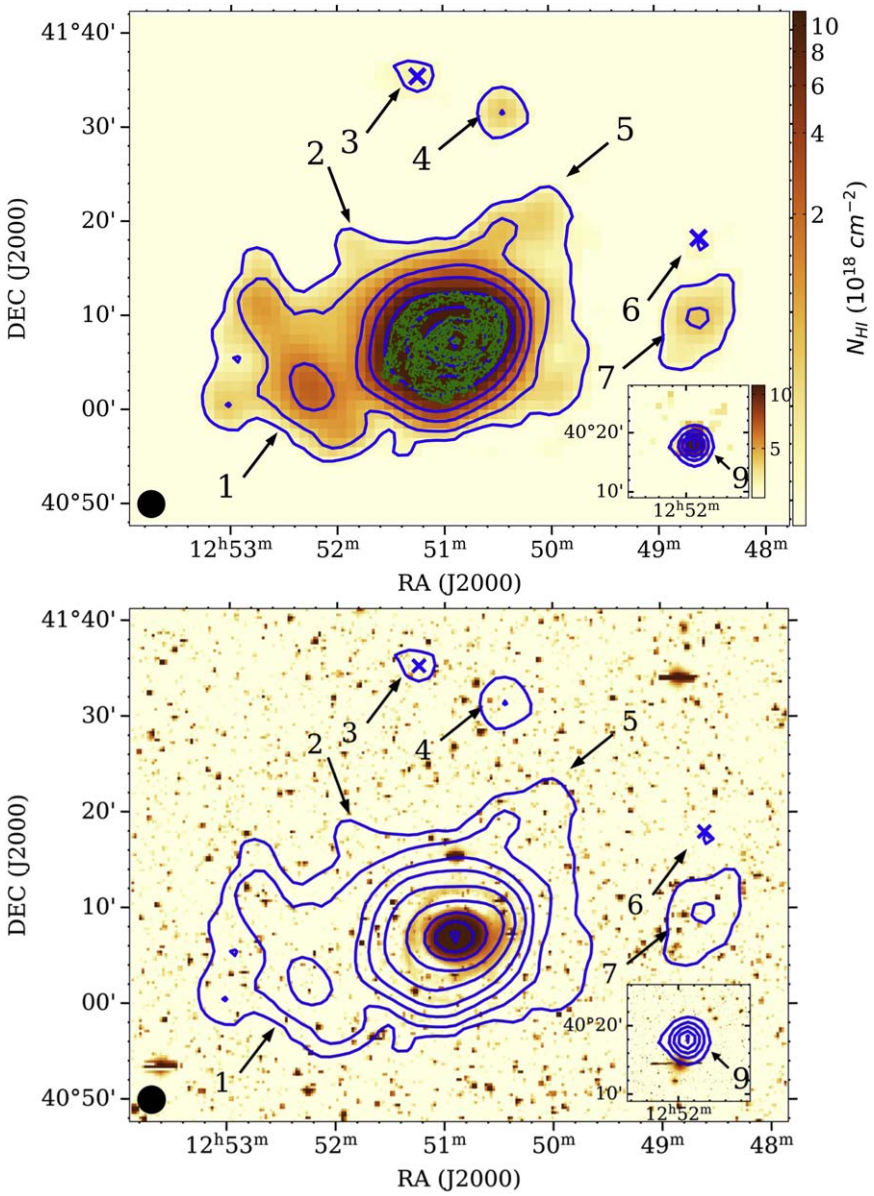

Figure 1. Top panel: the H I integrated intensity map of M94 region with the THINGS and FAST contours overlaid on it. The blue contours are FAST data integrated over 114–504 km s^{-1} and contour levels are 0.2, 0.7, 1.9, 4.4, 11.0, 21.0, 33.4, 45.8, and 58.3 × 10^{19} cm^{-2}. The green contours are THINGS images integrated over 144–490 km s^{-1}, and contour levels start at 1.3 × 10^{20} cm^{-2} and increments by 2.5 × 10^{20} cm^{-2}. Bottom: the same FAST contours overlaid on a DESI-LS optical image. The lower right-hand corner of both panels shows Cloud 9 integrated over 290–319 km s^{-1} with contour levels start at 6.7 × 10^{17} cm^{-2} in steps of 6.7 × 10^{17} cm^{-2}. The numbers represent names of the H I features indicated by the corresponding arrows. The crosses indicate possible features of HVC 3 and 6.

from the single dish measurement is missed by the THINGS map, due to the limited short spacing. To further reveal the flux difference, in the top panel of Figure 2 we compare the azimuth averaged surface density of flux profile of FAST and THINGS, and in the bottom panel we compare the accumulated flux profiles. Figure 2 clearly shows that the H I detected area of FAST is three times that of THINGS and most of the excess H I is distributed in the outskirts of M94 and not covered by the THINGS map.

3.3. Discovery of Discrete Clouds

Beside the extended disk, we see more diffuse H I structures outside the disk, which are marked with numbers 1–9 in Figure 1. Cloud 1 is a filament like structure, which could be debris of tidal tails. Clouds 2–7 are discrete clumps distributed around outskirt of M94, which appear to be similar to the high velocity clouds (HVCs) of the Milky Way (MW). Assuming a distance of 4.66 Mpc (Karachentsev 2005), the projected distance of these clouds is within 50 kpc from the center of M94. HVC 8 lies near the center of the disk, so it cannot be seen in the Figure 1 but can be clearly seen in the 382.34 km s^{-1} panel of the channel map (Figure 3), showing a counter-motion with respect to the disk rotation. Remarkably, we also detect a seemingly isolated H I cloud at a projected distance of 109 kpc south of M94 and name it Cloud 9, which is much farther from M94 than the MW's respective HVC population. On the FAST high-sensitivity image, we found no signs of a connection between this cloud and the M94 disk, at the column density level of 2.5 × 10^{18} cm^{-2} (3 σ). Thus, this cloud could be an isolated object. Indeed, clouds without relatively massive galaxies within a radius of 100 kpc are

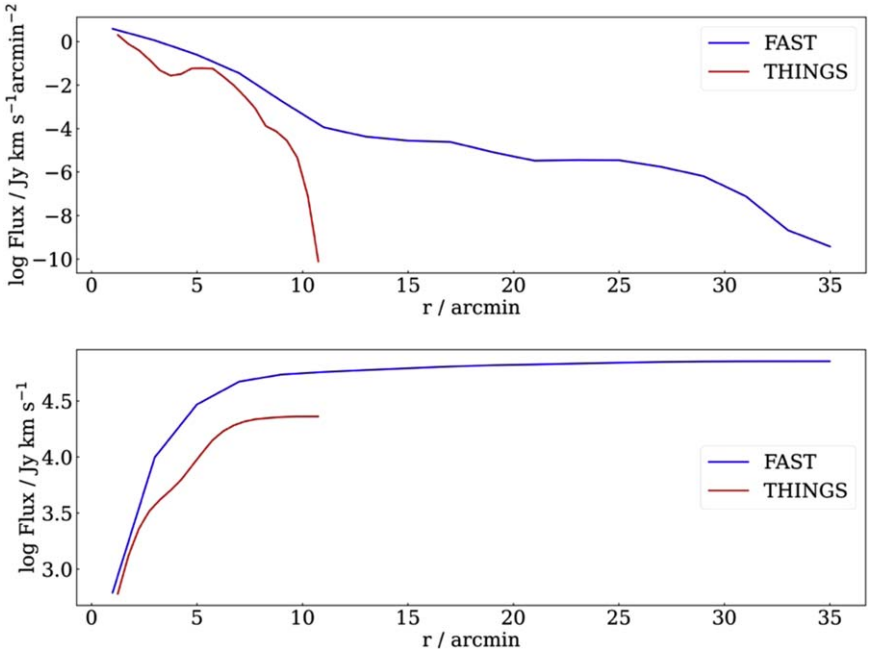

Figure 2. Top panel: The azimuth averaged flux profiles of FAST (blue curve) and THINGS map (red curve), which are varied with the distance from the center of M94. Bottom panel: the accumulated profile of flux of FAST (blue curve) and THINGS map (red curve) varied with the distance from the center of M94.

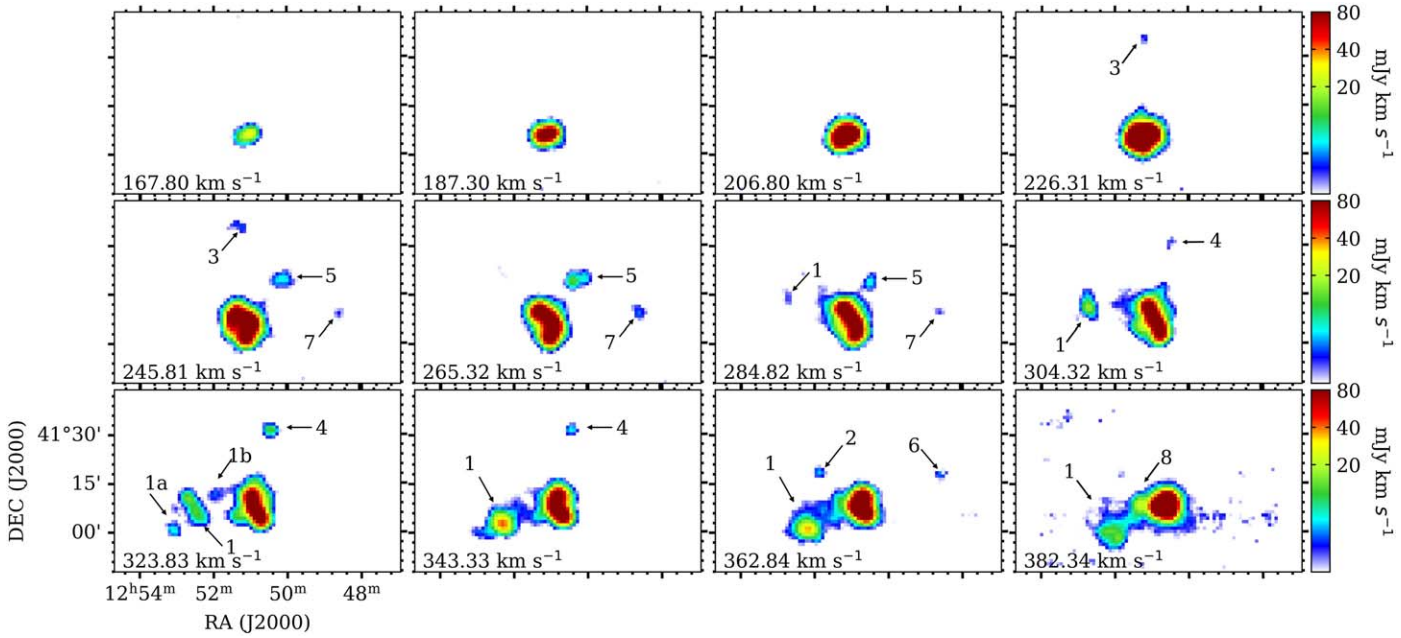

Figure 3. The FAST H I channel map of the M94 region. Each channel is integrated over a velocity range of 19.5 km s^{-1}. Arrows and numbers mark the names of H I features.

usually considered as isolated (Taylor et al. 2017). The details about Cloud 9 will be discussed in Section 4.2. Searching the DELCals images, we found that none of these H I features have optical counterparts. Table 1 lists the properties of these H I features. We use circles to approximate the size of the clouds, with the diameter of these circles listed in column (6). We use an ellipse to approximate H I filament 1, with its major and minor axis listed in column (6), respectively. Their flux is integrated within the extent of these ellipse and circles.

The channel map (Figure 3) focuses on the sky region of $191.^{\circ}89 < \alpha < 193.^{\circ}50$, $40.^{\circ}80 < \delta < 41.^{\circ}72$. It shows clear details of the H I filament 1 and HVCs 2–8. Although possible detections HVC 6 and 8 cannot be distinguished due to superposition in Figure 1, we can clearly see them in the channel map (Figure 3). Moreover, in the 323.83 km s^{-1} panel of Figure 3, there are two discrete clouds that seem to be connected with the H I filament and could be the substructures fragmented out of it, hence we mark them as 1a and 1b.

The top panel of Figure 4 shows the integrated flux density contours superimposed on the DESI-LS optical image for HVCs 3 and 6, and Cloud 9, which are integrated over the velocity range listed in Table 1. The FAST contours levels start at 3σ (8.1×10^{17}, 6.8×10^{17}, 6.7×10^{17} cm^{-2} for HVCs 3 and 6, and Cloud 9, respectively) in steps of 3σ. The bottom panels

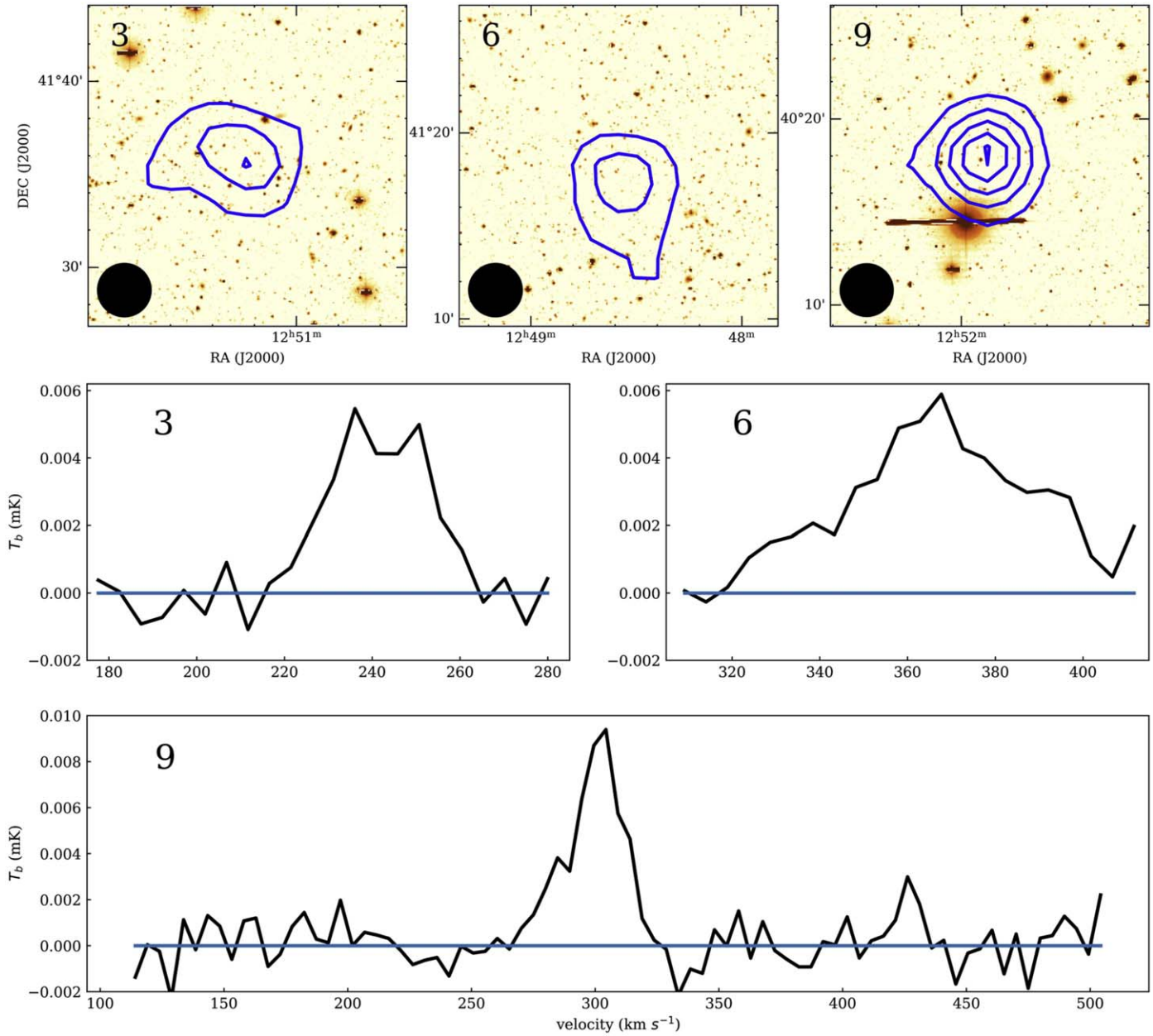

Figure 4. Top panel: the FAST integrated flux density contours of the H I detected by FAST superimposed on the DESI-LS optical image for HVCs 3 and 6, and Cloud 9, respectively, and the integrated velocity range is from Table 1. The contour levels start at 3σ (8.1×10^{17}, 6.8×10^{17}, 6.7×10^{17} cm^{-2} for HVCs 3 and 6, and Cloud 9 respectively) in steps of 3σ. FAST's HPBW is indicated in the bottom left-hand corner. Bottom: spectra taken at the peak column density of HVCs 3 and 6, and Cloud 9. The vertical axis is 21 cm brightness temperature and the horizontal axis is velocity.

show the spectra toward the peak column density of these clouds. The peak value of each cloud's spectra exceed 6σ. For Cloud 9, the S/N is as high as 9 and the profile of this cloud is the narrowest among the nine features.

3.4. H I Kinematics

The velocity field (moment-1) in the same region as the channel map is shown in Figure 5. Unlike other H I clouds, the H I filament 1 shows a velocity gradient. It is visible from 260.4 to 426.2 km s^{-1} in the form of a velocity gradient decreasing from the southwest to the northeast. The velocity field between the substructures 1a and 1b of the H I filament 1 are unchanged. Moreover, HVCs 2 and 5 are also discontinuous with the H I disk in velocity, as marked by the two black ellipses in Figure 5. In addition, we also made a moment-2 map[9] in Figure 6, which indicates the velocity dispersion. The moment-1 and moment-2 maps were also made using the spectral-cube algorithm and smoothed by a Gaussian filter (kernel=3×3). They were masked at 3σ of column density (2.5×10^{18} cm^{-2} for M94 region, and 6.7×10^{17} cm^{-2} for the lower right-hand subpanel) and a few obvious bad pixels were masked manually.

To explore the dynamic relationship of the H I filament and HVCs 2, 5 and 8, with M94, we made position–velocity (PV)

[9] Note that the spectral resolution of 4.88 km s^{-1} has not been corrected from this map. Thus, it cannot show any features with velocity dispersion smaller than 4.88 km s^{-1}.

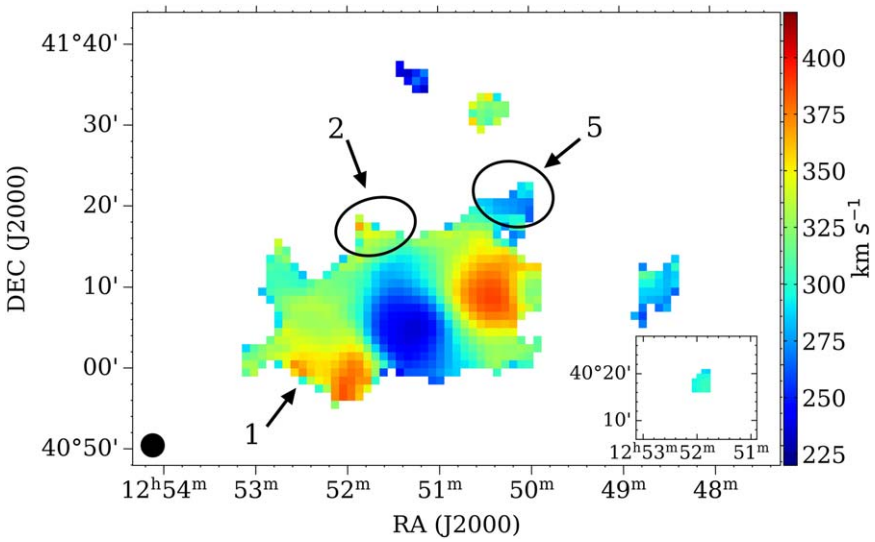

Figure 5. Velocity field of the M94 obtained from the H I data cube (moment-1 map). The black ellipses represent HVCs 2 and 5. FAST's HPBW is indicated in the bottom left-hand corner. The lower right-hand corner shows Cloud 9.

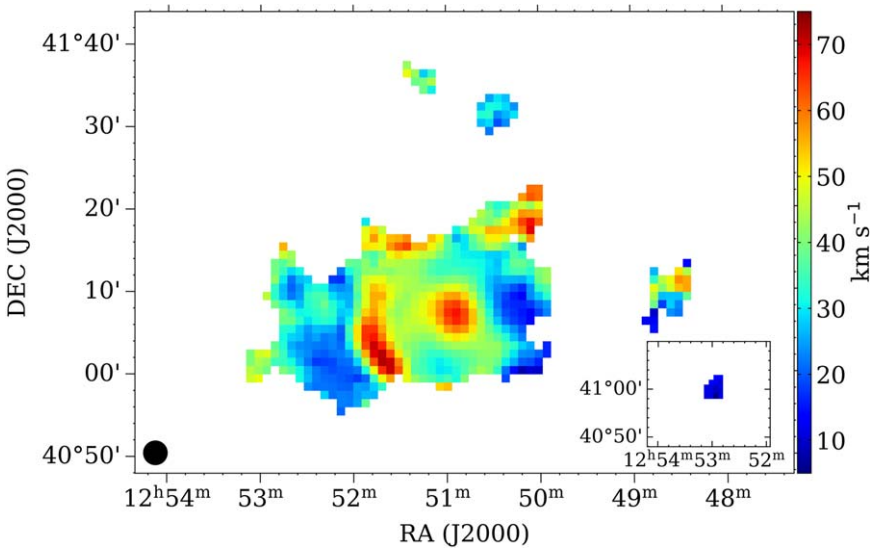

Figure 6. Velocity dispersion of the M94 obtained from the H I data cube (moment-2 map). FAST's HPBW is indicated in the bottom left-hand corner. The lower right-hand corner shows Cloud 9.

diagrams along different directions, which are shown in Figure 7. Panel (a) of Figure 7 shows the apparent velocity gradient of H I filament. From panel (d), we can see that the southwest of H I filament is not continuous with the H I disk in velocity, which can also be seen in Figure 5, although there is a gas connection between the H I filament and H I disk in the 343.33 to 382.34 km s^{-1} panels in Figure 3. Panel (b), (c), and (e) show that the velocity between HVCs 2, 5, and 8, and the H I disk is discontinuous. As for HVCs 3, 4, 6, and 7, they have similar projected distance to the H I disk, thus they could be remnants of an outer H I ring. The neutral gas connecting these clumps has disappeared or become undetectable now due to several reasons: either the gas disperses too faintly, or they are ionized by the inter-galactic UV radiation (Taylor et al. 2016). The existence of substructures 1a and 1b indicates that the H I filament 1 might start to fragment and can also eventually transform to discrete clumps due to dispersion or ionization.

4. Discussion

Compared with the THINGS observations (de Blok et al. 2008; Walter et al. 2008), we detected a more extended H I disk, and found a H I filament and seven HVCs within 50 kpc of the projection distance from the galactic center. We also found a seemingly isolated H I cloud that is located at the projection distance of 109 kpc from the galactic center, which may belong to M94. Here we consider the possible origins of these features.

4.1. Debris of Tidal Features in a Merger?

Figure 1 shows that the H I filament 1 appears to follow the spiral arm direction, like most tidal tails such as in the case of M51 (Rots et al. 1990), NGC 2535 (Kaufman et al. 1997), NGC 3893 (Verheijen & Sancisi 2001), and NGC 262 (Simkin et al. 1987). Moreover, the velocity field (Figure 5) is irregular

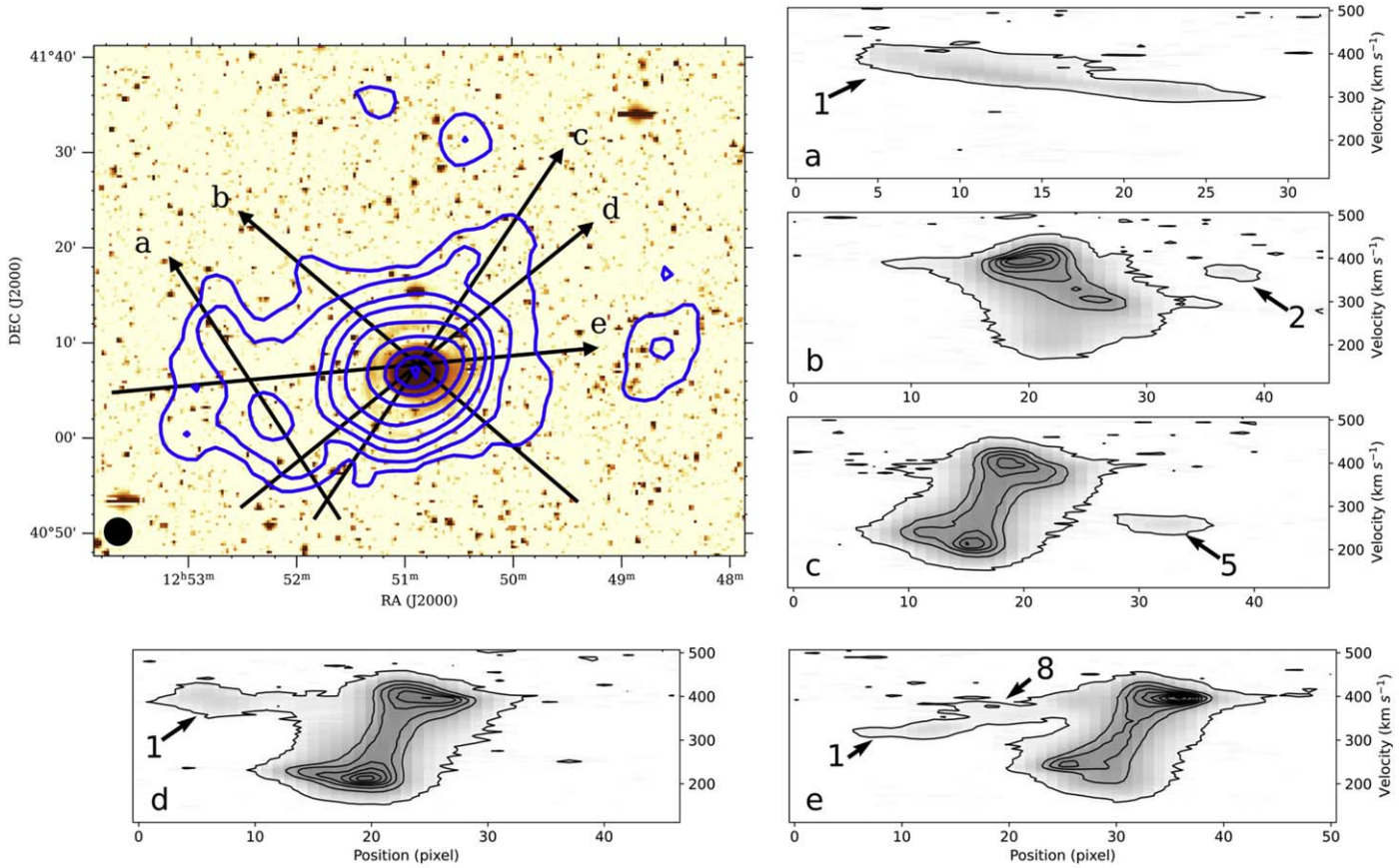

Figure 7. Four position–velocity plots along different directions. Top left-hand panel: the FAST H I integrated flux density contours in blue color overlaid on the DESI-LS optical image. The contour values are the same as those in Figure 1. The five black arrows mark the directions and positions of position–velocity diagrams in panels (a)–(e), respectively. FAST's HPBW is indicated in the bottom left-hand corner. Panels (a)–(e): the black contours start at 4σ (16.3 mJy) in steps of 80σ. Arrows and numbers mark the names of H I features.

Table 1
Properties of the H I Filament and Eight H I Structures

...	R.A.	Decl.	Velocity Range	Mean Velocity	Diameter	H I Flux	$M_{\rm H\,I}$
	hh:mm:ss	dd:mm:ss	km s^{-1}	km s^{-1}	arcmin	Jy km s^{-1}	$\times10^5 M_\odot$
(1)	(2)	(3)	(4)	(5)	(6)	(7)	(8)
1	12:51:42∼12:53:12	+40:54:30∼+41:17:33	260–426	355	11,26	5.646 ± 0.1	288.9 ± 5.0
2	12:51:52	+41:17:27	338–387	341	4	0.125 ± 0.005	6.4 ± 2.0
3	12:51:14	+41:35:28	226–260	248	4	0.100 ± 0.03	5.1 ± 1.0
4	12:50:24	+41:31:37	304–353	325	6	0.329 ± 0.003	16.8 ± 1.0
5	12:50:16	+41:19:22	231–314	292	8	0.714 ± 0.04	36.5 ± 2.0
6	12:48:35	+41:18:14	348–377	368	4	0.080 ± 0.04	4.1 ± 2.0
7	12:48:35	+41:09:12	245–294	285	8	0.683 ± 0.03	34.9 ± 2.0
8	12:51:20	+41:08:29	363–416	392	6	0.980 ± 0.1	50.1 ± 3.0
9	12:51:52	+40:17:29	290–319	298	6	0.239 ± 0.01	12.2 ± 0.5

Note. Columns 2 and 3: R.A. and decl. (J2000.0) are the R.A. and decl. the peak column density of each cloud respectively, expect H I filament, which is the position range. Column 4: velocity range is the range that the H I filament or clouds are visible. Column 5: mean velocity of H I structures. Column 6: diameter refers to the diameter of circles similar in size to clouds (major and minor axis, respectively, for an ellipse of H I filament 1). Column 7: H I flux is integrated within the extent of these ellipse and circles. Column 8: $M_{\rm H\,I}$ is the H I mass of the cloud, in solar masses, calculated by $M_{\rm H\,I}/M_\odot = 2.356\times10^5 D^2 S$, where D is the distance to the object in Mpc and S is the H I flux.

and disturbed at the position of the H I filament and HVCs 2 and 5. Such H I features without optical counterparts are often found surrounding interacting systems, e.g., NGC 7252 (Hibbard et al. 1994).

M94 has, however, a relatively isolated environment. It is located near the center of the Canes Venatici I cloud, which is a very loose extended system mainly including dwarf irregular galaxies. As the brightest galaxy of the CVn I cloud, M94 is the main disturber relating to only 10 neighboring galaxies (Karachentsev 2005). Most of the galaxies in this group seem to move with the expansion of the universe, which will prevent nearby collisions from affecting M94 (Karachentsev et al. 2003). So it seems unlikely for M94 to have recently had any interaction with other members of the group.

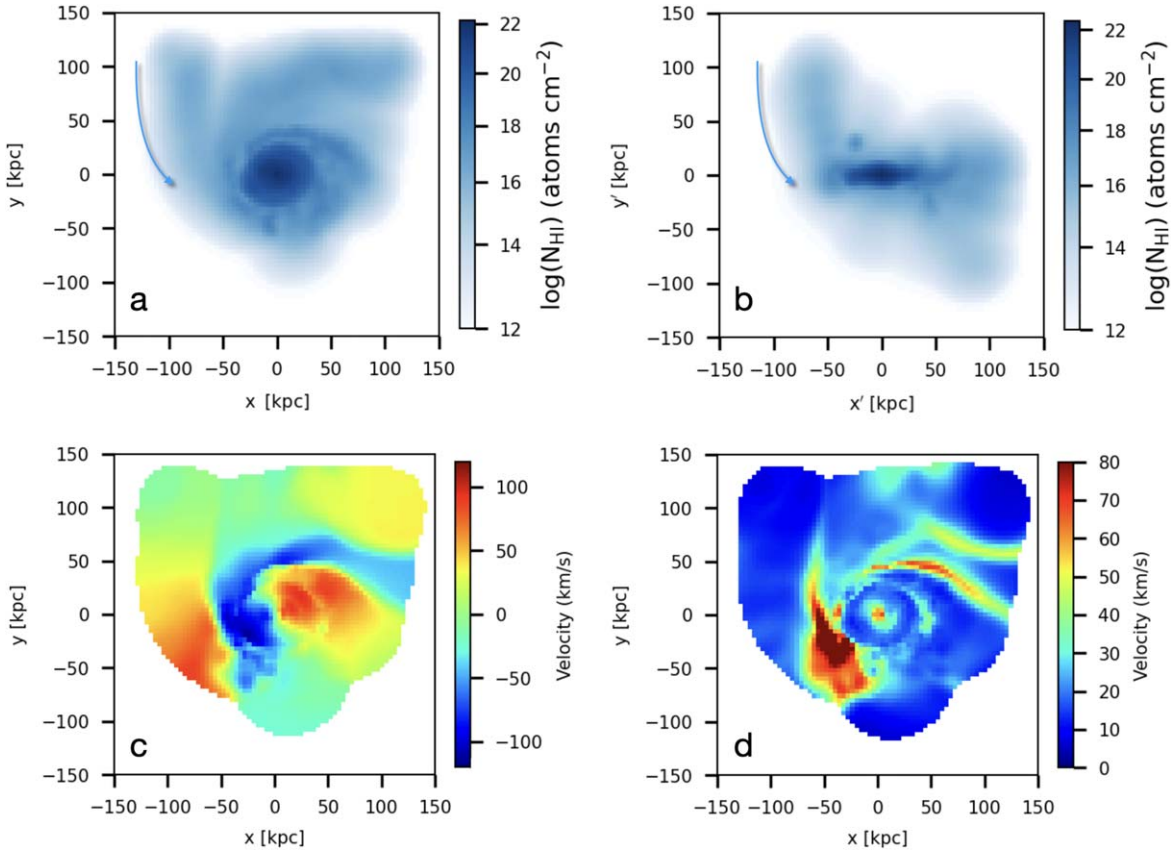

Figure 8. Morphology and kinematics of the simulated galaxy that are captured from the major merger model at 2 Gyr after the fusion of the two progenitors (see text for more details). The H I column density (panel (a)), the velocity field (panel (c)) and velocity dispersion map (panel (d)), projected at the observational view. Panel (b), the H I column density map projected along the edge-on view of the gas disk. The blue arrows in Panel (a) and (b) indicate the moving directions of the tidal tail from the secondary progenitor, respectively, in each projected plane.

As for the tidal encounters, Karachentsev et al. (2003) found no companions with a central surface brightness brighter than 25 $^{m}/\square''$ in the B-band within a radius of ∼3° or 230 kpc around M94. Although two satellites are found within 100 kpc of its projected distance, their M_* ($9.7 \times 10^5 M_\odot$ and $6.7 \times 10^5 M_\odot$; Smercina et al. 2018) is too low to drag these H I clouds out of the host galaxy. Moreover, there is an LSB galaxy LVJ 1243 + 4127 (Kim et al. 2020) at a distance of 4.75 ± 0.23 Mpc within 120 kpc projected distance of M94, whose mass is also too small to have a major impact. This leads to the idea that M94 may have undergone a past merger.

The global and large-scale morphology and kinematics of the diffuse gas outside the M94 appears similar to that of the M51. The H I features in the M51 system are thought to be the result of a very recent (∼ 250 Myr) galactic interaction (Yu et al. 2023). While M94 is seen as a single galaxy, with a giant stellar ring outside the optical disk (Trujillo et al. 2009) and a corresponding H I ring (Walter et al. 2008), could it be a remnant of the galaxy merger that is happening in M51?

To verify this idea, we turned back to the same simulation database as for the M51 system, i.e., the simulations carried out by Sauvaget et al. (2018) [10]. Specifically, we compare the period after the fusion of the two progenitor's cores. However, we notice that although the simulation for the M51 system could explain the disk and the ring of M94, it is unable to explain the kinematics of the filament, i.e., the H I filament 1. The simulation that could explain the observed properties of M94 H I gas is another model: "POLAR-RETPRO," which means that both galaxies have their disk highly inclined (71°) to the orbital plane (POLAR) and the large galaxy has a RETrograde disk rotation comparing to the angular momentum of the orbit while the second galaxy has a PROgrade rotation. The differences between the M51 model and the M94 model are the disk spins of progenitors with respect to the orbital angular momentum. It is indeed well-known that a polar type orbit favors the formation of a ring (e.g., Hammer et al. 2018).

Figure 8 shows the properties, i.e., the H I column density map and its kinematical maps, of the best-match epoch of the simulation, which is captured at 2 Gyr after the coalescence of the two progenitor's cores. All these maps are created with the same algorithms described in Yang et al. (2022). Specifically, here we adopted a grid resolution of 4 kpc in space and 5 km s^{-1} in velocity when creating the simulated "H I" data cube. The kinematics maps are obtained by flux-weighted mean in velocity and in dispersion, respectively.

The most peculiar and puzzling features in the observation are the kinematics of the filament (i.e., H I filament 1), which show completely different motions to the disk rotation of M94 (Figure 5). However, this becomes easy to understand if M94 was formed by a merger of two galaxies as an analog of the

[10] The authors have investigated a grid of representative simulations of gas-rich major mergers with a mass ratio of 3:1. The total initial baryon mass of the large galaxy is $5.3 \times 10^{10}\ M_\odot$ (52% in gas) and $1.76 \times 10^{10}\ M_\odot$ (72% in gas) for the small galaxy. Both galaxies are embedded in a dark matter halo, respectively, assuming a dark-to-baryon mass ratio of 4. The two progenitor disk galaxies are set on a parabolic orbit with a pericentre of 16 kpc.

model "POLAR-RETPRO" because the filament could be the tidal tail that was ejected at the first passage of the merger approximately 5 Gyr ago. Since then, the tidal tail continued to expand, with its near part (closer to M94) falling back and feeding the central region of M94. Due to the projection effect and also the initial geometric properties of the progenitors, i.e., the inclinations with respect to the orbital angular momentum, the tidal tail locates highly inclined (about 45°) to the central disk, as can be seen in Figure 8 when comparing the panel (a) and (b), for difference views of projection. This model could explain why the H I filament 1 shows a very distinct velocity distribution when compared to the central disk rotation. If the filament is the tidal tail in the model, then it would be located above the M94 disk and on the near side to us. As a result, we would observe the tidal tail falling toward the central disk, resulting in a velocity gradient from blue to redshift.

The idea that the filament (H I filament 1) could be a tidal tail instead being part of the extension of the central disk is supported further by the very high velocity dispersion region (Figure 6), which could be also explained by the simulation. The high velocity dispersion is caused by the superposition of the tidal tail and the outer part of the disk: their large contrast motions lead to high values when we calculate the dispersion in velocity. The infalling process of a tidal tail could last for several billion years or even longer, provided the tidal tail can survive the cosmic UV background radiation, for example.

If the H I filament and HVCs were formed simultaneously by the first passage of the merger 5 Gyr ago, then they may have undergone ionization as a result of photon ionization by young stars and the cosmic background. Moustakas et al. (2010) estimated the dimensionless ionization parameter (Tumlinson et al. 2011) of M94, which is $\log(U) \sim -3.04 \pm 0.24$. To estimate the neutral ratio of hydrogen ($N_{\rm H\,I}/N_{\rm H}$) of these H I features after 5 Gyr of photoionization, we take HVC 6 as an example, which has the lowest column density (2.04×10^{18} cm^{-2}). We fit the values of logU and $N_{\rm H\,I}$ of HVC 6 in the model in Figure 24 of Wang et al. (2023), and found that the resulting lower limit of $N_{\rm H\,I}$ is $1.8\%N_{\rm H}$, which indicates 5 Gyr of photoionization does not ionize all H I. Another effect that needs to be considered is the effect of evaporation. Using Equation (10) and similar parameters from Taylor et al. (2016), we estimated that only clouds with a radius of at least 26.8 kpc can survive after 5 Gyr evaporation time given the column density of the H I filament (7.91×10^{18} cm^{-2}). Thus, these HVCs should be remnant fragments of larger structures rather than isolated clouds initially. More than one tidal tail may be ejected at the first passage of the merger 5 Gyr ago, which dispersed into smaller clouds. We also estimate that after another 1.4 Gyr evaporation time, the H I filament 1 will disperse into smaller clouds and HVCs 2–8 will become too faint to be detected.

4.2. Possible Origins of Cloud 9

Cloud 9 is seemingly isolated, it may belong to M94, and its projection distance from the galactic center is 109 kpc. Its H I flux is 0.14 ± 0.02 Jy km s^{-1}, corresponding to a mass of $(7.2 \pm 1.0)\times10^5\,M_\odot$. The velocity width W_{50} of Cloud 9 is about 20 km s^{-1}. Adopting the Equation (2) from Wolfe et al. (2016), we take $r_{1/2} = 3.49$ kpc, FWHM = 20 km s^{-1}, and we estimate the dynamical (or viral) mass $M_{\rm dyn}$ of Cloud 9 as $3.49 \times 10^8\,M_\odot$. Here, we consider several possible origins of Cloud 9.

First, Cloud 9 could be tidal debris composed of pure gas without dark matter. In this case, the line width broadening is dominated by the gas temperature and is given by $T/{\rm K} = 21.8\,W_{50}^2$ with W_{50} given in km s^{-1}. Using $W_{50} = 20$ km s^{-1} yields a gas temperature $T\sim8.7\times10^3$K. Considering the distance between Cloud 9 and M94, it is not unusual to find tidal features longer than 100 kpc in merging systems (e.g., Appleton et al. 1987; Kent et al. 2007; Scott et al. 2012). Thus, it is possible to find tidal debris far away from the parent galaxies after merger. Based on the NGC 4490/85 system, Pearson et al. (2018) present a detailed theoretical model of the tidal encounter between two isolated low-mass galaxies. They demonstrated that baryons can be "parked" at very large distances by repeated encounters between two dwarf galaxies. If Cloud 9 originated from the same passage of the merger as other H I features, then the lower limit of its initial diameter should be 26.8 kpc according to the results of Section 4.1. Known H I streams could persist for several hundreds of Myr to a Gyr or more, but few H I stream can survive as long as 5 Gyr. For example, Oosterloo & van Gorkom (2005) suggest that a 100 kpc plume in Virgo has persisted for >100 Myr. The model of Michel-Dansac et al. (2010) implies that the formation of the Leo Ring begun 1.2 Gyr ago. If we consider the possibility that Cloud 9 is tidal debris that are the remnants of a long tidal tail, then 5 Gyr seems to be too long for it to survive. Meanwhile, mechanisms that involve star formation or dark matter, or both of them seem to be more ready to explain the long survival time of Cloud 9, as discussed in the following.

Second, Cloud 9 may be a dark dwarf galaxy, such as a low surface brightness (LSB) galaxy. The optical detection limits of DESI-LS are 29.15 mag arcsec^{-2} in g, 28.73 mag arcsec^{-2} in r, and 27.52 mag arcsec^{-2} in z (Martínez-Delgado et al. 2023). Adopting the method from Zhu et al. (2021), we estimated that Cloud 9 would not be brighter than 25.66 mag in g, 25.24 mag in r and 24.03 mag in z, with the disk scale length $R_s = 0.080$ kpc and the major-to-minor axis ratio $q = 1$. So Cloud 9 would not be brighter than 26.03 mag in the B-band as estimated with equation $m_B = m_g + 0.47(m_g - m_r) + 0.17$ (Smith et al. 2002). We can further derive that the lower limit absolute B-band magnitude (M_B) is 2.31 mag and the upper limit B-band luminosity is $1.26\times10^3\,L_\odot$ obtained with $L_B = D^2 10^{10-0.4(m_B - M_{B0})}$, where M_{B0} is the absolute solar B-band magnitude adopted as 5.44 mag (Willmer 2018). Moreover, we estimated that the upper limit stellar mass of Cloud 9 is $1.14\times10^5\,M_\odot$, with the g-r color value and B-band luminosity (Zhang et al. 2017). We can calculate the baryonic mass ($M_{\rm bar}$) of the probable dark galaxy associated with Cloud 9 by $M_{\rm bar} = M_* + M_{\rm gas}$, where M_* is the stellar mass and $M_{\rm gas}$ is the total gas mass. We can ignore the contribution of the stellar mass to the baryonic mass of Cloud 9 because it is too small. Assuming the same helium-to-H I ratio as that obtained from big bang nucleosynthesis, the total gas mass ($M_{\rm gas}$) is determined by $M_{\rm gas} = 1.33 \times M_{\rm H\,I}$. Thus, the baryonic mass of Cloud 9 is about $9.58\times10^5\,M_\odot$. The dynamical mass to total baryonic mass ratio is derived to be about 364, implying that dark matter absolutely dominates over baryons in Cloud 9. We used the Baryonic Tully–Fisher relation (BTF) to explore the properties of the probable dark galaxy Cloud 9, which is an empirical correlation for disk galaxies. This dark galaxy is gas-dominated, but it nearly follows the best-fit relation $M_{\rm bar} = AV_{\rm rot}^4$ with $A = 47 \pm 6\ M_\odot\,{\rm km}^{-4}{\rm s}^4$ for gas-dominated

disk galaxies (McGaugh 2012) and $V_{\rm rot} = 1/2$ FWHM. This implies that Cloud 9 may be hosting a normal dwarf disk galaxy.

Third, Cloud 9 may also be a mini dark matter halo that is only composed of gas and dark matter, and hence it is invisible in optical. Supposing that it is in virial equilibrium, then it is sensible to equal M_{200} [11] to $M_{\rm dyn}$. Cloud 9 may be a starless gaseous minihalo of present-day mass in the range $10^6 \lesssim M_{200}/M_\odot \lesssim 5 \times 10^9$, in which the gas is in thermal equilibrium with the UV background radiation and in hydrostatic equilibrium in the gravitational potential of the halo, i.e., a RELHIC object (Benítez-Llambay et al. 2017; Benitez-Llambay & Frenk 2020). Cloud 9 conforms to several properties of RELHICs in the Local Group proposed by Benítez-Llambay et al. (2017): (i) it is nearly round on the sky (b/a >.8 at 1×10^{18} cm^{-2}), (ii) with a small (sub-kpc) neutral hydrogen core, and (iii) a very narrow distribution of thermally broadened line widths ($W_{50} \sim 20$ km s^{-1}). If Cloud 9 was a RELHIC, then it provides a robust prediction of the CDM paradigm and is a great example to explore the RELHICs outside the Local Group.

Comparing these three origins of Cloud 9, we prefer the dark dwarf galaxy and RELHIC scenarios rather than tidal debris based on the estimated long survival time of this cloud.

5. Conclusion

In conclusion, we have obtained a deep H I image for the vicinity of M94 with FAST and discovered much more diffuse H I structures. Major new features are listed in the following:

1. A more extended H I disk.
2. A H I filament and seven HVCs, whose projected distance from the galactic center is within 50 kpc.
3. A seemingly isolated Cloud 9 at the projection distance of 109 kpc.

With the complex morphology and kinematics, we suggest that M94 is likely a remnant of a major merger of two galaxies. To explain the observed properties of M94 H I gas, we simulated it with the model: "POLAR-RETPRO. The best-match epoch of the simulation is captured at 2 Gyr after the coalescence of the two progenitor's cores. We suggest that the H I filament could be the tidal tail ejected at the first passage of the merger 5 Gyr ago. The HVCs could be fragments of larger structures such as tidal tails that originated at the same time as the H I filament. We consider several possible origins for the nearly isolated Cloud 9, especially the dark dwarf galaxy and RELHIC scenarios. The former is expected to contribute considerably to our understanding of the low-mass and ultra-faint galaxies. The detection and characterization of the latter would provide a novel opportunity to reveal the dark side of a CDM-dominated universe. In optical images, M94 is such an isolated galaxy with few signs of interaction. Thus, high-sensitivity H I imaging is important in revealing the diffuse H I structures and tidal debris, which is crucial to understanding the dynamical evolution of galaxies.

Acknowledgments

We thank the FAST staff for help with the FAST observations. We thank Dr. Francois Hammer for his helpful discussion. We acknowledge the support of the National Key R&D Program of China (2018YFE0202900; 2017YFA0402600). We also thank the National Natural Foundation of China (NSFC Nos. 12041302 and 11973042) and also the support of the International Research Program (IRP) Tianguan, which is an agreement between the CNRS, NAOC, and the Yunnan University.

[11] We define M_{200} as the mass calculated within a radius with mean inner density equals 200 times the critical density of the universe, $\rho_{\rm crit} = 3H^2/8\pi G$.

ORCID iDs

Ruilei Zhou https://orcid.org/0009-0009-0581-5237
Ming Zhu https://orcid.org/0000-0001-6083-956X
Yanbin Yang https://orcid.org/0000-0001-7949-3407
Haiyang Yu https://orcid.org/0000-0001-9838-7159
Lixia Yuan https://orcid.org/0000-0003-0804-9055
Peng Jiang https://orcid.org/0000-0002-5387-7952

References

Appleton, P. N., Ghigo, F. D., van Gorkom, J. H., et al. 1987, Natur, 330, 140
Baek, S.-J., Park, A., Ahn, Y.-J., et al. 2015, Ana, 140, 250
Barnes, D. G., Staveley-Smith, L., de Blok, W. J. G., et al. 2001, MNRAS, 322, 486
Benitez-Llambay, A., & Frenk, C. 2020, MNRAS, 498, 4887
Benítez-Llambay, A., Navarro, J. F., Frenk, C. S., et al. 2017, MNRAS, 465, 3913
Braun, R. 1995, A&AS, 114, 409
Buta, R. J., Corwin, H. G., Jr, & Odewahn, S. C. 2007, The de Vaucouleurs Atlas of Galaxies. (Cambridge: Cambridge Univ. Press)
Constantin, A., & Seth, A. C. 2012, AdAst, 2012, 178060
de Blok, W. J. G., Walter, F., Brinks, E., et al. 2008, AJ, 136, 2648
de Vaucouleurs, G., de Vaucouleurs, A., Corwin, H. G., Jr., et al. 1991, Third Reference Catalogue of Bright Galaxies (New York: Springer)
Dey, A., Schlegel, D. J., Lang, D., et al. 2019, AJ, 157, 168
Hammer, F., Yang, Y. B., Wang, J. L., et al. 2018, MNRAS, 475, 2754
Herrmann, K. A., & Ciardullo, R. 2009, ApJ, 705, 1686
Herrmann, K. A., Ciardullo, R., & Sigurdsson, S. 2009, ApJL, 693, L19
Hibbard, J. E., Guhathakurta, P., van Gorkom, J. H., et al. 1994, AJ, 107, 67
Hopkins, P. F., Cox, T. J., Younger, J. D., et al. 2009, ApJ, 691, 1168
Jarrett, T. H., Chester, T., Cutri, R., et al. 2003, AJ, 125, 525
Jiang, P., Tang, N.-Y., Hou, L.-G., et al. 2020, RAA, 20, 064
Jiang, P., Yue, Y., Gan, H., et al. 2019, SCPMA, 62, 959502
Karachentsev, I. D. 2005, AJ, 129, 178
Karachentsev, I. D., Sharina, M. E., Dolphin, A. E., et al. 2003, A&A, 398, 467
Kaufman, M., Brinks, E., Elmegreen, D. M., et al. 1997, AJ, 114, 2323
Kent, B. R., Giovanelli, R., Haynes, M. P., et al. 2007, ApJL, 665, L15
Kim, Y. J., Kang, J., Lee, M. G., et al. 2020, ApJ, 905, 104
Kinney, A. L., Bohlin, R. C., Calzetti, D., et al. 1993, ApJS, 86, 5
Körding, E., Colbert, E., & Falcke, H. 2005, A&A, 436, 427
Maoz, D., Filippenko, A. V., Ho, L. C., et al. 1995, ApJ, 440, 91
Maoz, D., Nagar, N. M., Falcke, H., et al. 2005, ApJ, 625, 699
Martínez-Delgado, D., Roca-Fàbrega, S., Miró-Carretero, J., et al. 2023, A&A, 669, A103
McGaugh, S. S. 2012, AJ, 143, 40
Michel-Dansac, L., Duc, P.-A., Bournaud, F., et al. 2010, ApJL, 717, L143
Moustakas, J., Kennicutt, R. C., Tremonti, C. A., et al. 2010, ApJS, 190, 233
Mulder, P. S. 1995, A&A, 303, 57
Muñoz-Tuñón, C., Caon, N., & Aguerri, J. A. L. 2004, AJ, 127, 58
Nan, R., Li, D., Jin, C., et al. 2011, IJMPD, 20, 989
Oosterloo, T., & van Gorkom, J. 2005, A&A, 437, L19
Pearson, S., Privon, G. C., Besla, G., et al. 2018, MNRAS, 480, 3069
Peñarrubia, J., McConnachie, A., & Babul, A. 2006, ApJL, 650, L33
Roberts, T. P., Schurch, N. J., & Warwick, R. S. 2001, MNRAS, 324, 737
Rots, A. H., Bosma, A., van der Hulst, J. M., et al. 1990, AJ, 100, 387
Sauvaget, T., Hammer, F., Puech, M., et al. 2018, MNRAS, 473, 2521
Scott, T. C., Cortese, L., Brinks, E., et al. 2012, MNRAS, 419, L19
Shioya, Y., Tosaki, T., Ohyama, Y., et al. 1998, PASJ, 50, 317
Simkin, S. M., Su, H.-J, & van Gorkom, J. 1987, Sci, 235, 1367
Smercina, A., Bell, E. F., Price, P. A., et al. 2018, ApJ, 863, 152
Smith, B. J., Lester, D. F., Harvey, P. M., et al. 1991, ApJ, 373, 66
Smith, J. A., Tucker, D. L., Kent, S., et al. 2002, AJ, 123, 2121
Taylor, R., Davies, J. I., Jáchym, P., et al. 2016, MNRAS, 461, 3001
Taylor, R., Davies, J. I., Jáchym, P., et al. 2017, MNRAS, 467, 3648

Trujillo, I., Martinez-Valpuesta, I., Martínez-Delgado, D., et al. 2009, ApJ, 704, 618
Tumlinson, J., Werk, J. K., Thom, C., et al. 2011, ApJ, 733, 111
Velazquez, H., & White, S. D. M. 1999, MNRAS, 304, 254
Verheijen, M. A. W., & Sancisi, R. 2001, A&A, 370, 765
Waller, W. H., Fanelli, M. N., Keel, W. C., et al. 2001, AJ, 121, 1395
Walter, F., Brinks, E., de Blok, W. J. G., et al. 2008, AJ, 136, 2563
Wang, J., Yang, D., Oh, S.-H., et al. 2023, ApJ, 944, 102
Watkins, A. E., Mihos, J. C., & Harding, P. 2016, ApJ, 826, 59
Willmer, C. N. A. 2018, ApJS, 236, 47
Wolfe, S. A., Lockman, F. J., & Pisano, D. J. 2016, ApJ, 816, 81
Xu, J.-L., Zhang, C.-P., Yu, N., et al. 2021, ApJ, 922, 53
Yang, Y., Ianjamasimanana, R., Hammer, F., et al. 2022, A&A, 660, L11
Yu, H., Zhu, M., Xu, J.-L., et al. 2023, MNRAS, 521, 2719
Zhang, H.-X., Puzia, T. H., & Weisz, D. R. 2017, ApJS, 233, 13
Zhu, M., Yu, H., Wang, J., et al. 2021, ApJL, 922, L21